Ferroelectric Diodes with Charge Injection and Trapping

Zhen Fan,[1,*] Hua Fan,[1] Zengxing Lu,[2] Peilian Li,[1] Zhifeng Huang,[1] Guo Tian,[1] Lin Yang,[1] Junxiang Yao,[1] Chao Chen,[1] Deyang Chen,[1] Zhibo Yan,[2] Xubing Lu,[1] Xingsen Gao,[1,†] and Jun-Ming Liu[1,2]

[1]*Institute for Advanced Materials and Guangdong Provincial Key Laboratory of Quantum Engineering and Quantum Materials, South China Normal University, Guangzhou 510006, China*

[2]*Laboratory of Solid State Microstructures and Innovation Center of Advanced Microstructures, Nanjing University, Nanjing 210093, China*

(Received 8 September 2016; revised manuscript received 4 November 2016; published 27 January 2017)

Ferroelectric diodes with polarization-modulated Schottky barriers are promising for applications in resistive switching (RS) memories. However, they have not achieved satisfactory performance reliability as originally hoped. The physical origins underlying this issue have not been well studied, although they deserve much attention. Here, by means of scanning Kelvin probe microscopy we show that the electrical poling of ferroelectric diodes can cause significant charge injection and trapping besides polarization switching. We further show that the reproducibility and stability of switchable diode-type RS behavior are significantly affected by the interfacial traps. A theoretical model is then proposed to quantitatively describe the modifications of Schottky barriers by charge injection and trapping. This model is able to reproduce various types of hysteretic current-voltage characteristics as experimentally observed. It is further revealed that the charge injection and trapping can significantly modify the electroresistance ratio, RS polarity, and high- or low-resistance states initially defined by the polarization direction. Several approaches are suggested to suppress the effect of charge injection and trapping so as to realize high-performance polarization-reversal-induced RS. This study, therefore, reveals the microscopic mechanisms for the RS behavior comodulated by polarization reversal and charge trapping in ferroelectric diodes, and also provides useful suggestions for developing reliable ferroelectric RS memories.

DOI: 10.1103/PhysRevApplied.7.014020

I. INTRODUCTION

Ferroelectric resistive memories have emerged as an attractive candidate for next-generation nonvolatile memory technology, owing to the promise of subnanosecond switching speed, high read-write endurance cycles, low power consumption, and nondestructive readout [1–5]. They can be further categorized into two types according to the mechanism variance. One is the ferroelectric tunnel junctions, in which an ultrathin ferroelectric layer acts as a tunneling barrier and the tunneling resistance can be modulated by the polarization. The other is the ferroelectric diodes utilizing the polarization to tune the interface Schottky barriers. Because ferroelectric resistive memories are based on polarization-reversal-induced resistive switching (RS), high reliability seems to be taken for granted. Unfortunately, ferroelectric resistive memories often show poor reproducibility and device-to-device variability [6–9], severely hindering the practical applications. To address these issues, a thorough understanding of the origin underlying the huge diversity of RS phenomena is urgently needed [10]. This paper, therefore, aims to investigate the fundamentals of ferroelectric RS effects and will mainly deal with the physics of ferroelectric diodes.

Ferroelectric diodes were first developed in $Au/PbTiO_3/La_{0.5}Sr_{0.5}CoO_3$ heterostructures by Blom *et al.* [11] in 1994. It was observed that the polarization-induced band bending could change the $Au/PbTiO_3$ contact from the Schottky type to the Ohmic type, thus giving rise to a resistance change of 2 orders of magnitude. Pintilie *et al.* [12,13] developed a theoretical model for ferroelectric diodes. Their model adapted classic theories of Schottky contacts for ferroelectric diodes by treating the polarization as a charge sheet [12]. This model fairly described the experimentally observed current-voltage (I-V) and capacitance-voltage (C-V) characteristics of ferroelectric diodes [13]. Recently, switchable diode effects coupled with tunable photovoltaic responses were discovered in $BiFeO_3$ single crystals [4,14] and thin films [5,15], and since then there has been a boost in the number of studies on ferroelectric diodes.

While previous studies were largely concerned with the effect of polarization reversal on RS, much less attention was paid to other possible effects, e.g., those caused by defects. Indeed, according to the theories of ferroelectric diodes [12,13], ionic defects are indispensable, as they

*To whom all correspondence should be addressed. fanzhen@m.scnu.edu.cn

†To whom all correspondence should be addressed. xingsengao@scnu.edu.cn

could render the ferroelectric layer semiconducting. This is the prerequisite for forming a Schottky barrier. The charges at ionic defects (either donors or acceptors) in the space-charge region (SCR) are compensated by the polarization charges. Hence, the width of SCR could be modulated by the polarization, resulting in tunable Schottky barriers and a switchable diode effect. Without these defects, the ferroelectric layer will be insulating and the switchable diode-type RS behavior could be weak in spite of good ferroelectricity [9]. Given the presence of the charged defects, however, common defect-mediated RS mechanisms, like migration of oxygen vacancies and charge trapping and detrapping, may also exist [16,17]. The overall RS behavior is therefore a consequence of the competition between polarization-modulated RS and defect-mediated RS. For example, it was recently found that $BiFeO_3$ with *p*-type semiconducting characteristics arising from Bi deficiencies could exhibit the polarization-controlled switchable diode effect [18–20], whereas oxygen vacancy-rich *n*-type $BiFeO_3$ shows only the conventional bipolar RS behavior irrelevant to polarization [20]. Along this line, it is of great importance to figure out the roles of polarization and defects in ferroelectric diodes and their respective impacts on the RS behavior. In this regard, most previous studies still remain at a qualitative level, while a quantitative model on ferroelectric diodes taking into account the defect-mediated RS mechanisms is still lacking. Such a quantitative model may be helpful for guiding a delicate control of defects so as to achieve high reliability and reproducibility in ferroelectric diodes.

Among various defect-mediated RS mechanisms, the charge injection and trapping effect will be mainly focused in this study. The charge injection and trapping are likely to occur because the ionic defects in the SCR of ferroelectric diodes may create deep trap states, which can capture the charge carriers injected from the electrodes. The charge trapping has a great impact on RS and this has been widely reported in transitional metal oxides [21]; however, it has not received due attention in ferroelectric diodes, although it may be closely related to the aforementioned issues of reliability and reproducibility [22]. Herein, we report a systematic study of polarization reversal and charge-trapping comodulated RS behavior in ferroelectric diodes. We first demonstrate by using scanning Kelvin probe microscopy (SKPM) that upon an electrical poling, the charge injection and trapping do occur concurrently with the domain switching. Then, we present evidence that the reproducibility and stability of switchable diode-type RS behavior are significantly influenced by the interfacial traps. Based on the experimental observations and previous theories [12,13], we develop a model of ferroelectric diodes involving the effect of charge injection and trapping. This model quantitatively reveals how both polarization and trapped charges modify the Schottky barriers and, consequently, influence the RS behavior.

II. EXPERIMENTAL METHODS AND RESULTS

In our experiments, ferroelectric $BiFeO_3$ (BFO) thin films with the thickness of ∼40 nm are deposited on $La_{0.7}Sr_{0.3}MnO_3$ (LSMO)-buffered $SrTiO_3$ (001) substrates by pulsed laser deposition at a temperature of 680 °C and an oxygen pressure of 15 Pa. The crystal structures of the deposited films are characterized by x-ray diffraction (XRD) and reciprocal space mappings (RSMs). The XRD θ-2θ diffraction patterns in combination with the (103) and (113) RSMs demonstrate that both the BFO and LSMO films are fully strained (see Fig. S1 in the Supplemental Material [23]). In addition, the BFO unit cell exhibits a c/a ratio of ∼1.04 and a monoclinic tiling angle of ∼1.3°.

For the electrical measurements, the top Au electrodes with different sizes are tested. The large-area Au electrodes (200 μm in diameter) are deposited by conventional sputtering using a shadow mask, while nanoelectrodes with an area of <0.05 μm^2 each are prepared using a polystyrene spheres template [24]. It is found that the large-area Au electrodes are not suitable for electrical measurements, because of the leakage issues caused by the conductive filaments (although the BFO bulk matrix could still have a good quality; see Fig. S2 in the Supplemental Material [23]). Electrical conduction through the filaments also makes the switchable diode-type RS behavior unobservable since the conduction mechanism in this case is no longer the interface-controlled Schottky emission. Therefore, to avoid the effect of the conductive filaments, nanoelectrodes are used in this study.

The SKPM and piezoresponse force microscopy (PFM) are conducted using a scanning probe microscope (Cypher, Asylum Research). The PFM characterizes the domain structures and the local domain switching behavior. The SKPM measures the surface potential, which depends on the relative amounts of polarization charges and screening charges [25]. It is known that there are mainly three types of screening charges: (i) charged species (either electronic or ionic) within the film that are migrated towards the surface region, (ii) surface adsorbates, and (iii) injected charges that are trapped at the surface. Upon an electrical poling, the injected charges often become the dominating part of the screening charges [26].

In our experiments, two adjacent areas are electrically poled with ±5 V, respectively, for subsequent observations. After the poling, the topography, PFM phase, and SKPM surface-potential images are recorded. Figure 1(a) shows almost no morphological changes in the poled regions, thus denying the occurrence of electrochemical reactions. The PFM phase image in Fig. 1(b) shows that the BFO domains are switched into two opposite orientations after the ±5 V poling. Meanwhile, the +5 V (−5 V) poled region shows increased (decreased) surface potential compared with the as-grown region [Fig. 1(c)]. Here, it should be mentioned that in the absence of screening charges, the

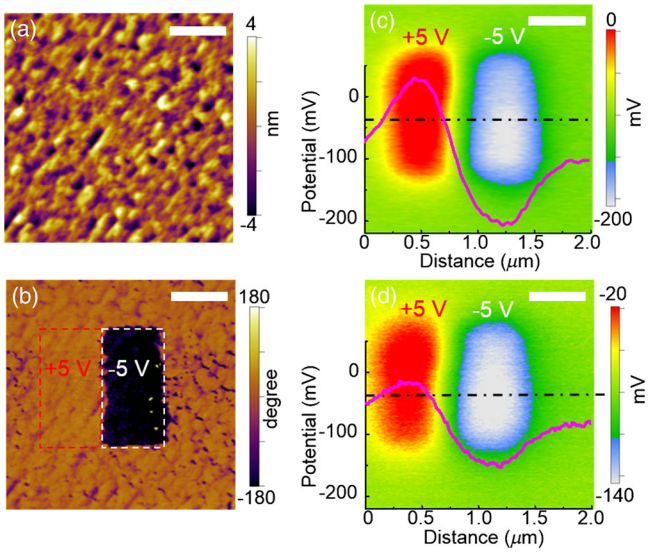

FIG. 1 (a) Topography, (b) PFM phase, and (c) SKPM surface-potential images of BFO films after ±5 V poling in two adjacent areas. (d) SKPM surface-potential image taken after grounded-tip scanning.

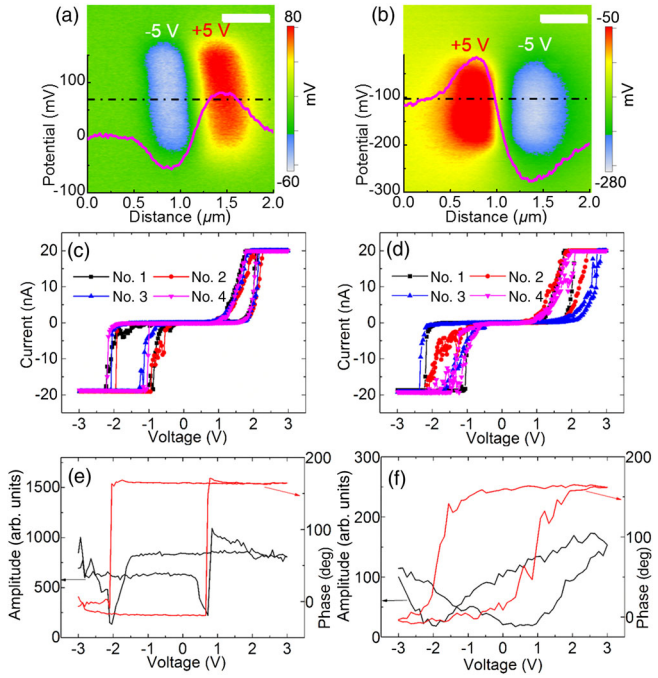

FIG. 2. SKPM results of (a) as-grown and (b) plasma-treated samples. *I-V* curves are measured in different devices for (c) as-grown and (d) plasma-treated samples. PFM phase (red line) and amplitude (black line) hysteresis loops are measured for (e) as-grown and (f) plasma-treated samples.

negative (positive) polarization charges attracted to the surface by the +5 V (−5 V) poling will lead to the surface-potential variations opposite to what have been observed. This suggests that the polarization charges are overcompensated by the screening charges, and more specifically, the injected charges (confirmed by the poling voltage-dependent SKPM and PFM results; see Fig. S3 in the Supplemental Material [23]). After the film is poled with +5 V (−5 V), holes (electrons) are injected from the tip and trapped at the surface, and they can even overcompensate the negative (positive) polarization charges. This will cause the surface-potential variations, consistent with the SKPM results. The SKPM image taken after the grounded-tip scanning [Fig. 1(d)] shows that the contrasts between the poled and as-grown regions still remain in spite of a certain degree of decay. The persisted surface-potential differences suggest that some of the injected charges are captured by deep traps and are thus difficult to remove. Therefore, it has been demonstrated that the electrical poling induces not only polarization switching but also charge injection and trapping. Similar observations have been reported in a wide variety of ferroelectrics [27,28].

To qualitatively show the influence of charge injection and trapping on the transport properties, the *I-V* characteristics are measured for two different samples. One is the as-grown sample while the other one is treated by the O_2 plasma with a power of 15 W and a pressure of ∼10 mtorr for 20 min. The O_2 plasma treatment causes almost no changes in the sample surface morphology (see Fig. S4 in the Supplemental Material [23]). However, more defects are generated in the surface regions (see Fig. S5 in the Supplemental Material [23]), perhaps due to the ion bombardment during the plasma treatment [29,30]. These defects can also induce an increased density of surface states (also acting as the interfacial traps), and therefore the effect of charge injection and trapping in the plasma-treated sample is more significant. This has been confirmed by the SKPM results. As seen from Figs. 2(a) and 2(b), the surface-potential changes induced by ±5 V poling in the plasma-treated sample are much larger than those in the as-grown sample, indicating that more charges are trapped in the surface regions of the plasma-treated sample. Then, *I-V* curves are swept within ±3 V on the Au nanoelectrodes of the two different samples. Figure 2(c) presents the *I-V* curves measured on different electrodes of the as-grown sample, and they all exhibit similar switchable diode-type RS behaviors. However, for the plasma-treated sample, the *I-V* curves with various shapes are observed and the representative results are shown in Fig. 2(d). These *I-V* curves may be classified into four types: (i) a conventional switchable diode, (ii) hysteresis only in the positive branch, (iii) hysteresis only in the negative branch, and (iv) negligible hysteresis. In addition, for a specific device with the plasma-treated sample, the *I-V* curves vary irregularly in the cycling tests (results not shown here), indicating a poor RS stability. It is noted that the domains in both samples can be fully switched at ±3 V [Figs. 2(e) and 2(f)], thus excluding the incomplete domain switching as one possible origin of the great diversity of *I-V* hysteresis in the

plasma-treated sample. It may therefore be deducible that the charge injection and trapping greatly influence the RS behavior of the plasma-treated sample which is confirmed to have a high density of interfacial traps.

III. THEORETICAL MODEL

Given the experimental confirmation of the existence of charge injection and trapping and its influence on the transport properties of ferroelectric diodes, we then develop a theoretical model of polarization reversal and charge-trapping comodulated ferroelectric diodes. Several assumptions which set the basis for the present model will be made as follows, and most of them were already employed in the model of Pintilie *et al.* [12].

(1) A ferroelectric layer is either a p-type or an n-type semiconductor depending on the defect chemistry. Taking the p-type ferroelectric layer as an example, it can form a Schottky barrier with a low-work-function metal. The effective charge density (N_{eff}) in the SCR of a Schottky barrier consists of both shallow- and deep-level acceptors. Note these deep-level acceptors need to be distinguished from the deep traps that will be introduced later, because the deep-level acceptors can still be ionized once the quasi-Fermi-level is above the deep acceptor level.

(2) A metal-ferroelectric-metal (MFM) structure may be regarded as two back-to-back Schottky diodes [Fig. 3(a)] or a single diode plus an Ohmic contact [Fig. 3(b)]. The ferroelectric layer is thick enough to avoid the overlapping of two SCRs in the back-to-back diode model (or larger than the SCR width in the single-diode model). The neutral regions outside SCRs are assumed to have negligible resistances.

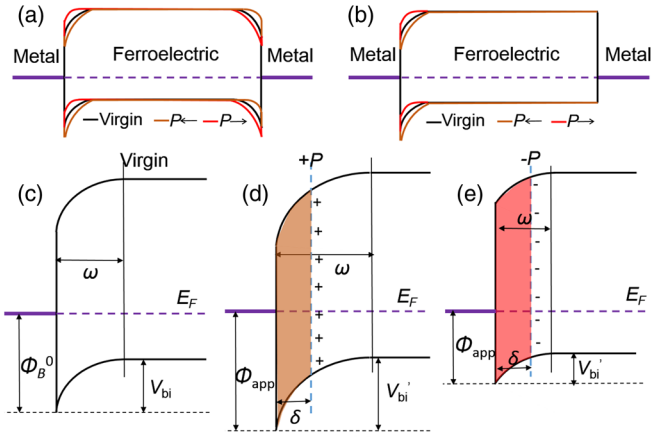

FIG. 3. Schematics showing (a) back-to-back diode and (b) single-diode models. Energy-band diagrams of a Schottky diode in (c) virgin (without polarization and trapped charges), (d) negatively poled, and (e) positively poled states. The trapped electrons and holes in the dead layer are shaded in brown and red, respectively. Note that the apparent Schottky barriers sketched by the bold black lines are the barriers seen by the electrons and holes in the thermionic emission process, and they are not the real potential energy profiles.

(3) The polarization is treated as a charge sheet located in the ferroelectric layer, which is separated from the metal-ferroelectric interface by a so-called dead layer. This dead layer may have a large number of deep traps besides the shallow- and deep-level acceptors. These traps can be assumed to be uniformly distributed in the dead layer with a density of N_T. They are able to capture both electrons and holes, according to previous theories [31] and our experimental observations. It may be conveniently assumed that the empty traps are neutral but they become negatively (positively) charged if electrons (holes) are trapped [31]. The charge-trapping effect at the interface of an Ohmic contact can be safely neglected because the charge carriers are rather free to move from electrodes to the ferroelectric layer or vice versa. Thus, we consider only the charge-trapping effect in the Schottky contacts.

(4) Polarization switching as well as charge injection and trapping are assumed to occur instantly under the same switching field (i.e., coercive field E_c), and there will be no changes of polarization and trapped charges except at E_c. To be more specific, upon the application of $+E_c$ ("+" denotes the direction from top to bottom), negative (positive) polarization charges are attracted to the top (bottom) interface (i.e., $P\downarrow$), and holes (electrons) are also trapped at the top (bottom) dead layer. Both the polarization and trapped charges remain unchanged unless the electric field changes to $-E_c$. At $-E_c$, the polarization will be reversed (i.e., $P\uparrow$), and originally trapped holes (electrons) will be detrapped and subsequently those traps will be refilled with electrons (holes). This "ideal switching" assumption is made because it is very difficult to simulate the electric field-dependent behaviors of polarization switching and charge injection and trapping. In addition, the time-dependent characteristics of charge injection and trapping are not considered because they are quite elusive. In the equilibrium state, the total amount of charges induced by polarization and dielectric response is

$$\sigma_{\text{tot}} = \varepsilon_0 \varepsilon_{\text{st}} E_c + P, \tag{1}$$

where ε_0 and ε_{st} are the vacuum permittivity and static dielectric constant, respectively. If all of these charges are assumed to be injected from the electrodes to the ferroelectric layer, the amount of charges trapped at the dead layer may be

$$Q_{\text{trapped}} = qN_{\text{trapped}}\delta = \min(\sigma_{\text{tot}}, qN_T\delta), \tag{2}$$

where q is the electron charge, N_{trapped} is the number of trapped charge carriers, and δ is the dead-layer thickness.

(5) The measured I-V characteristics are assumed to be quasistatic. The transient currents at $\pm E_c$ arising from the polarization switching and charge injection are not taken

into account. The *I-V* characteristics may be conveniently described by the thermionic emission model [12]. However, in a realistic MFM structure, the mean free paths of the injected charge carriers are often smaller than the film thickness. The conduction mechanism is therefore no longer a pure thermionic emission. The overall conduction process consists of an interface-controlled injection, followed by a low-mobility drift through the film volume. This may be adequately described by the Schottky-Simmon model [32]. The difference between the Schottky-Simmons equation and the thermionic emission equation lies in the preexponential term [32]. In the Schottky-Simmons equation, the preexponential term depends on the electric field E and carrier mobility μ [see Eq. (14) in Ref. [32]]. However, it is revealed that the dependence of the preexponential term on E is rather weak [32]. Therefore, the Schottky-Simmons equation is similar in form to the thermionic emission equation. The thermionic emission equation may be applicable to simulate the *I-V* characteristics, but one has to bear in mind that the Richardson constant A^* being used is a factor related to the drift-diffusion process. Nevertheless, the values of A^* will not affect the most concerned resistive switching properties, e.g., electroresistance (ER) ratios.

We first introduce the concept of apparent built-in potential ($V'_{\rm bi}$) in the present model [12]. Because of the presence of polarization and trapped charges, the built-in potential as employed in the conventional Schottky barrier ($V_{\rm bi}$) should be replaced with the apparent built-in potential $V'_{\rm bi}$ [Figs. 3(c)–3(e)]. By further using the Gauss's law and Poisson's equation, $V'_{\rm bi}$ can be derived from $V_{\rm bi}$ as

$$V'_{\rm bi} = V_{\rm bi} \mp \frac{P}{\varepsilon_0\varepsilon_{\rm st}}\delta \pm \frac{qN_{\rm trapped}}{2\varepsilon_0\varepsilon_{\rm st}}\delta^2. \tag{3}$$

In Eq. (3), the lower signs apply to the case of the negatively poled Schottky barrier, where the $P\uparrow$ state is established and electrons are injected from the electrode and subsequently trapped in the dead layer [Fig. 3(d)]. In contrast, the upper signs in Eq. (3) apply to the reverse case, i.e., the positively poled Schottky barrier [Fig. 3(e)]. The $V_{\rm bi}$ in Eq. (3) is linked with the Schottky barrier height at zero field (Φ_B^0) by

$$V_{\rm bi} = \Phi_B^0 - \frac{kT}{q}\ln\left[\frac{N_V}{p(T)}\right], \tag{4}$$

where k is the Boltzmann's constant, T is the temperature, N_V is the effective density of states for holes in the valence band, and $p(T)$ is the hole concentration at the temperature T. N_V is determined by the hole effective mass (m_h^*) and temperature T as

$$N_V = 2\left[\frac{2\pi m_h^* kT}{h^2}\right], \tag{5}$$

where h is the Planck constant.

The SCR width ω can be derived from the apparent built-in potential $V'_{\rm bi}$ as

$$\omega = \sqrt{\frac{2\varepsilon_0\varepsilon_{\rm st}(V + V'_{\rm bi})}{qN_{\rm eff}}}, \tag{6}$$

where V is the applied bias. According to assumption (2), the SCR width is narrower than half of the film thickness $d/2$ in the back-to-back diode model (d in the single-diode model). On the other hand, the SCR width could not be too small; otherwise, conduction mechanisms other than thermionic emission, such as tunneling, will be involved. We, therefore, set the lower limit of ω as δ. Hence, the boundary conditions of ω are

$$\delta \le \omega \le \frac{d}{2} \quad (\text{or } d \text{ in the single-diode model}). \tag{7}$$

The maximum field at the interface (E_m) is then given by

$$E_m = \frac{qN_{\rm eff}}{\varepsilon_0\varepsilon_{\rm st}}\omega \pm \frac{P}{\varepsilon_0\varepsilon_{\rm st}} \mp \frac{qN_{\rm trapped}}{\varepsilon_0\varepsilon_{\rm st}}\delta. \tag{8}$$

Again, the upper signs apply to the positively poled Schottky barrier while the lower signs apply to the negatively poled one.

The current density arising from thermionic emission of a reverse-biased Schottky barrier is expressed as

$$J = A^*T^2\exp\left[-\frac{q}{kT}\left(\Phi_B^0 - \sqrt{\frac{qE_m}{4\pi\varepsilon_0\varepsilon_{\rm op}}}\right)\right], \tag{9}$$

where A^* is the Richardson's constant and $\varepsilon_{\rm op}$ is the optical dielectric constant. An apparent Schottky barrier height ($\Phi_{\rm app}$) can be defined as [32]

$$\Phi_{\rm app} = \Phi_B^0 - \sqrt{\frac{qE_m}{4\pi\varepsilon_0\varepsilon_{\rm op}}}. \tag{10}$$

Hereinafter, the barrier height as mentioned refers to $\Phi_{\rm app}$. The current density of a forward-biased Schottky barrier is given by

$$J = A^*T^2\exp\left(-\frac{q\Phi_{\rm app}}{kT}\right)\exp\left(\frac{qV}{nkT}\right), \tag{11}$$

where n is the ideality factor and it reflects the barrier-height variation induced by the applied voltage V [33]. Therefore, V may not need to be included in the expression of $\Phi_{\rm app}$ for a forward-biased Schottky barrier.

IV. SIMULATED RESULTS AND DISCUSSION

Based on the above model, we simulate the transport properties of several conventional ferroelectric materials, including $Pb(Zr,Ti)O_3$ (PZT), $PbTiO_3$ (PTO), $BaTiO_3$ (BTO), $SrBi_2Ta_2O_9$ (SBT), and BFO. In the following of this study, PZT with *p*-type character will be mainly focused due to the convenience of accessing all the relevant parameters for calculations [13]. BFO will be less focused because some parameters of BFO are absent. For example, the effective charge density N_{eff} of our BFO films could hardly be measured using the conventional *C-V* method, owing to the ultrasmall electrodes being used. Large-area electrodes are also not suitable for the *C-V* measurements given the leakage issue caused by conductive filaments. Nevertheless, using PZT rather than BFO as an example will not affect the general applicability of our model.

The simulated *I-V* characteristics of a PZT back-to-back diode model with different N_{trapped} are shown in Fig. 4. In the simulation, besides the basic parameters of PZT listed in Table I, $d = 200$ nm, $\delta = 3$ nm, $A^* = 520\,\text{A}\,\text{cm}^{-2}\,\text{K}^{-2}$, and $p\ (T = 300\ \text{K}) = 5 \times 10^{18}\ \text{cm}^{-3}$ are used [13]. $N_{\text{eff}} = 9.92 \times 10^{20}\ \text{cm}^{-3}$, the maximum value allowed by the constraint of Eq. (7), is also used. As seen from Fig. 4(a), conventional switchable diode behavior is observed if the influence of charge injection and trapping is not considered [4,5,15]. This can be understood by the fact that the top Schottky barrier will be higher when the MFM structure is in the $P\uparrow$ state and thus the hole transport will be more difficult under positive bias. As the electric field reaches +2 V (corresponding to $+E_c$), the polarization switching occurs, leading to the $P\downarrow$ state. The top Schottky barrier height will be reduced and thus the hole transport will be facilitated under the positive bias. Therefore, a transition from the high-resistance state (HRS) to the low-resistance state (LRS) is observed at +2 V in the positive branch of the *I-V* curve [Fig. 4(a)]. The *I-V* hysteresis in the negative branch can be analyzed in the same way. In the presence of $N_{\text{trapped}} = 4.5 \times 10^{20}\ \text{cm}^{-3}$, however, the *I-V* hysteresis almost disappears [Fig. 4(b)]. When N_{trapped} further increases to $9 \times 10^{20}\ \text{cm}^{-3}$, the *I-V* hysteresis reappears, but its RS polarity becomes the opposite [LRS → HRS at ±2 V; see Fig. 4(c)]. This type of RS polarity reversal is an indicator that the RS is caused by the charge injection and trapping at both interfaces [43]. These results, therefore, show that as N_{trapped} increases, the trapped charges will suppress and further dominate over the polarization charges in inducing RS. The reason is that the trapped charges modify the key parameters of a Schottky barrier, such as $V_{\text{bi}}^{'}$ and E_m, in a way opposite to polarization charges [see Eqs. (3) and (8)]. Note that in real ferroelectric perovskite thin films, the trap density N_T could reach $\sim 10^{21}\ \text{cm}^{-3}$ [44]. In addition, the charge injection is able to supply a carrier density of $\sim 10^{21}\ \text{cm}^{-3}$ according to Eq. (1). Therefore, the values of N_{trapped} used in our calculations may be reasonable.

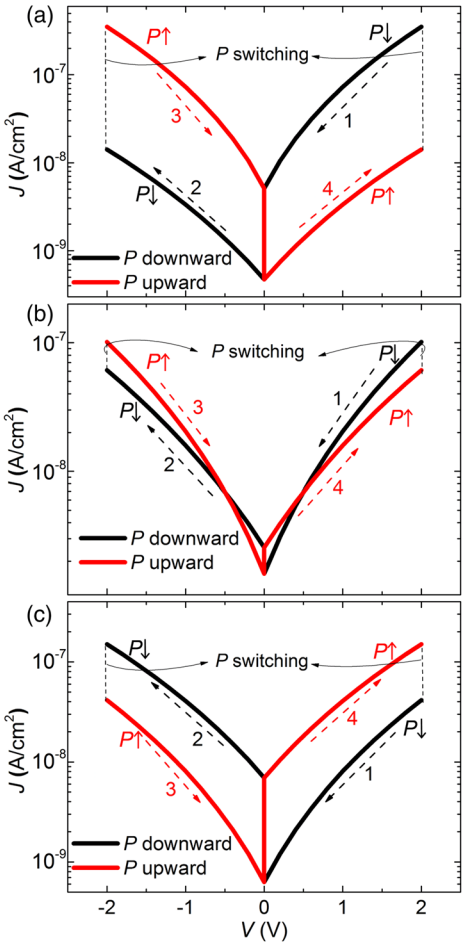

FIG. 4. *I-V* characteristics of a PZT back-to-back diode model with (a) $N_{\text{trapped}} = 0$, (b) $N_{\text{trapped}} = 4.5 \times 10^{20}\ \text{cm}^{-3}$, and (c) $N_{\text{trapped}} = 9 \times 10^{20}\ \text{cm}^{-3}$.

Figure 5 shows the *I-V* characteristics of the PZT single-diode model, which are simulated using the same parameters adopted in the back-to-back diode model. Unlike the back-to-back diode model, there is only one Schottky barrier (the top one is assumed) limiting the conduction in the single-diode model. Therefore, the current rectifying direction remains unchanged, although the barrier height may vary. In addition, the imprint effect (i.e., the shift of E_c) caused by the asymmetric interface barriers is neglected. As shown in Fig. 5(a), at $N_{\text{trapped}} = 0$, the RS behavior with a "countereightwise" polarity is observed. To be more specific, $P\uparrow$ ($P\downarrow$) results in a HRS (LRS) in both positive and negative voltage regimes, because $P\uparrow$ ($P\downarrow$) induces a higher (lower) top Schottky barrier for the hole transport under both reverse and forward bias conditions. This observation is consistent with that reported in Ref. [45]. As N_{trapped} increases to $4.5 \times 10^{20}\ \text{cm}^{-3}$, however, the *I-V* hysteresis becomes almost negligible [Fig. 5(b)]. At $N_{\text{trapped}} = 9 \times 10^{20}\ \text{cm}^{-3}$, the RS behavior with an "eightwise" polarity appears [Fig. 5(c)]. This is a

TABLE I. Basic parameters of different ferroelectric materials used for calculations.

Material	P (μC/cm^2)	E_c (kV/cm)	ε_{st}	ε_{op}	Φ_B^0 (eV)/electrode
PZT[a]	40	400	180	6.5	1.3/$SrRuO_3$
PTO	80[b]	280[b]	130[b]	6.25[c]	1.5[c]/Pt
BTO	~30[d]	150[d]	500[e]	6.1[c]	~1.5[f]/Au and LSMO
SBT	10[g]	40[g]	400[g]	5.3[c]	1.2[c]/Pt
BFO	~60[h]	200[h]	100[i]	6.25[j]	~0.9[k]/Pt and $SrRuO_3$

[a]See Ref. [13].
[b]See Ref. [34].
[c]See Ref. [35].
[d]See Ref. [36].
[e]See Ref. [37].
[f]See Ref. [9].
[g]See Ref. [38].
[h]See Ref. [39].
[i]See Ref. [40].
[j]See Ref. [41].
[k]See Ref. [42].

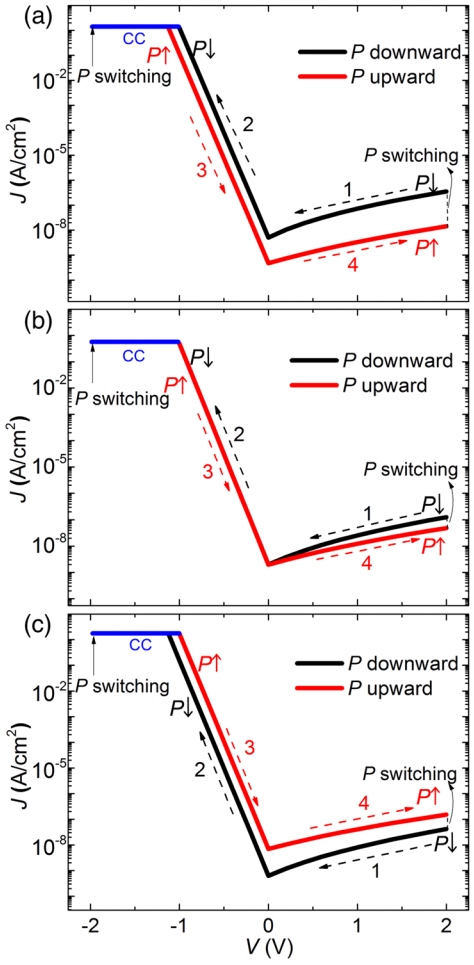

FIG. 5. I-V characteristics of a PZT single-diode model with (a) $N_{trapped} = 0$, (b) $N_{trapped} = 4.5 \times 10^{20}$ cm^{-3}, and (c) $N_{trapped} = 9 \times 10^{20}$ cm^{-3}. Here, CC denotes compliance current.

typical feature of charge trapping at one of the interfaces in a MFM structure [46–48]. Therefore, the charge-trapping-induced RS gradually masks the polarization-induced RS as $N_{trapped}$ increases, which is similar to what has been observed in the back-to-back diode model.

The above results may help explain the poor reproducibility and stability of RS behavior observed in our plasma-treated sample which has a high density of interfacial traps. Because the amount and location (either or both interfaces) of trapped charges can vary in different devices and even in different switching cycles, the resultant I-V curves may have a wide variety of shapes [Fig. 2(d)].

We then focus our attention on the ER ratio of ferroelectric diodes under the influence of charge injection and trapping. The ER ratio is defined as the ratio of $J(P\downarrow; V_{read} = 1\ V)$ versus $J(P\uparrow; V_{read} = 1\ V)$. The PZT back-to-back diode model is used as an example. Figure 6(a) reveals that the initial ER ratio higher than 1 can be continuously tuned to be even lower than 1 as $N_{trapped}$ increases. This means that the HRS and LRS initially defined by the polarization state can be reversed when the charge injection and trapping occur. Next, one may be interested in how to engineer the effective charge density (N_{eff}) and the deep trap density (N_T) to achieve the best performance of polarization-reversal-induced RS. Figure 6(b) shows the ER ratio as a function of N_{eff} at different N_T. Here, all traps are assumed to be filled, i.e., $N_{trapped} = N_T$. At $N_T = 0$, the ER ratio increases with decreasing N_{eff}. This may be interpreted by the fact that the polarization-induced variation in the SCR width will be larger when N_{eff} becomes smaller [see Eq. (6)]. The resultant variation in the apparent barrier height (Φ_{app}) will also be larger. However, when N_t is large, e.g., 1.35×10^{21} cm^{-3}, smaller N_{eff} will lead to a more significant ER ratio reduction caused by charge injection and trapping. At a moderate N_T, e.g., 7.2×10^{20} cm^{-3}, there is

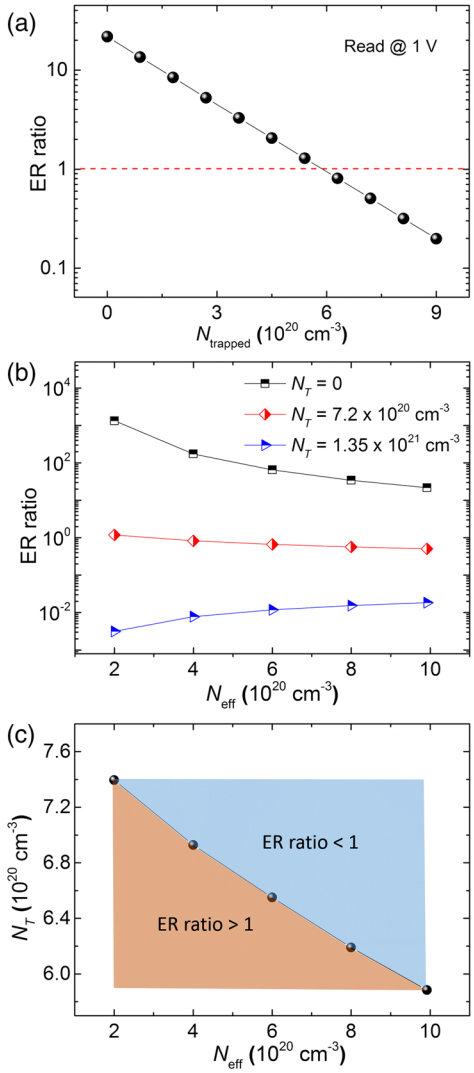

FIG. 6. (a) ER ratio as a function of N_{trapped} and (b) ER ratio as a function of N_{eff} under the conditions of different N_T. (c) Critical N_T at ER ratio $= 1$ as a function of N_{eff}. All parameters used here are the same as those used for calculations in Fig. 4 unless specifically stated.

not much change in the ER ratio as N_{eff} varies. Therefore, to achieve a high ER ratio of polarization-reversal-induced RS, the deep traps need to be minimized to the greatest extent first, and then N_{eff} is also reduced under the constraint of Eq. (7). Figure 6(c) shows that the critical N_T at ER ratio $= 1$ increases as N_{eff} decreases. This implies that decreasing N_{eff} can tolerate more deep traps to be present without changing the HRS and LRS defined by the polarization state.

It is also of great interest to study how the properties of the dead layer influence the RS behavior. The dead-layer thicknesses (δ) often vary in different metal-ferroelectric interfaces, e.g., Pt/BFO, and this has been proposed to be one of the major origins of different RS behaviors observed in Pt/BFO/$SrRuO_3$ heterostructures [18]. As shown in Fig. 7(a), the polarization-reversal-induced RS behavior becomes more significant as the dead-layer thickness δ decreases. For all δ being investigated, the ER ratios modified by the full-charge injection and trapping ($qN_{\text{trapped}}\delta = \sigma_{\text{tot}}$) are all below 1 and they decrease as δ increases. This suggests that the charge-trapping-induced RS could be suppressed by decreasing δ, which was experimentally demonstrated in Pt/Nb:$SrTiO_3$ heterostructures [49,50]. Therefore, keeping δ as small as possible is beneficial not only for achieving large ER ratios of polarization-reversal-induced RS, but also for suppressing the interference from charge injection and trapping.

Because the static dielectric constant of the dead layer ($\varepsilon_{\text{st\_}d}$) is often lower than that of the bulk region ($\varepsilon_{\text{st\_}b}$) [51], the dependence of ER ratio on $\varepsilon_{\text{st\_}d}$ needs to be investigated. In this case, Eqs. (3) and (8) need to be modified as

$$\frac{qN_{\text{eff}}}{2\varepsilon_0\varepsilon_{\text{st\_}b}}\omega_b^2 + \frac{qN_{\text{eff}}}{2\varepsilon_0\varepsilon_{\text{st\_}d}}\delta^2 + \frac{qN_{\text{eff}}}{\varepsilon_0\varepsilon_{\text{st\_}d}}\omega_b\delta = V'_{\text{bi}} = V_{\text{bi}} \mp \frac{P}{\varepsilon_0\varepsilon_{\text{st\_}d}}\delta \pm \frac{qN_{\text{trapped}}}{2\varepsilon_0\varepsilon_{\text{st\_}d}}\delta^2, \tag{12}$$

$$E_m = \frac{qN_{\text{eff}}}{\varepsilon_0\varepsilon_{\text{st\_}d}}\omega_b + \frac{qN_{\text{eff}}}{\varepsilon_0\varepsilon_{\text{st\_}d}}\delta \pm \frac{P}{\varepsilon_0\varepsilon_{\text{st\_}d}} \mp \frac{qN_{\text{trapped}}}{\varepsilon_0\varepsilon_{\text{st\_}d}}\delta, \tag{13}$$

respectively. Here, ω_b is the width of SCR in the bulk region. As shown in Fig. 7(b), smaller $\varepsilon_{\text{st\_}d}$ leads to a larger ER ratio for polarization-reversal-induced RS. However, smaller $\varepsilon_{\text{st\_}d}$ also makes the interference from charge injection and trapping more severe. The reduction of $\varepsilon_{\text{st\_}d}$ leading to more significant charge-trapping-induced RS has been observed in metal-Nb:$SrTiO_3$ junctions [52]. Therefore, an appropriate $\varepsilon_{\text{st\_}d}$ is needed to optimize the RS behavior that is simultaneously influenced by polarization and trapped charges.

We finally investigate the material dependence of polarization reversal and charge-trapping comodulated RS behavior. As can be seen from Fig. 7(c), PTO and BFO, which have the largest polarizations (see Table I), show the highest ER ratios when N_{trapped} is 0. However, their ER ratios are most significantly reduced under the condition of full-charge injection and trapping. This is because a large polarization gives a large σ_{tot} according to Eq. (1), thus leading to a large N_{trapped} if the full-charge injection and trapping occur ($qN_{\text{trapped}}\delta = \sigma_{\text{tot}}$).

Based on the above results, some effective approaches are suggested to suppress the effect of charge injection and trapping and thus realize high-performance polarization-reversal-induced RS:

(i) Using materials with large polarization to achieve large modulation of Schottky barriers by polarization
(ii) Minimizing the deep trap density (N_T), which is a straightforward way to reduce the amount of trapped charges
(iii) Keeping the effective charge density (N_{eff}) small, which can amplify the variation of SCR width

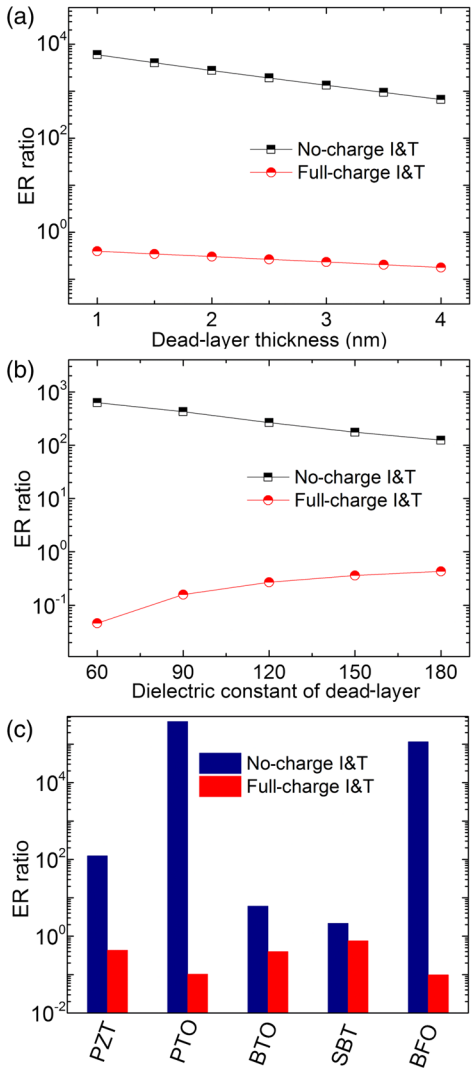

FIG. 7. ER ratio with and without the influence of charge injection and trapping as a function of (a) dead-layer thickness δ, (b) dielectric constant of dead layer ε_{st_d}, and (c) type of material. Here, "No-charge I&T" corresponds to $N_{trapped} = 0$ while "Full-charge I&T" corresponds to $qN_{trapped}\delta = \sigma_{tot}$. In panel (a), $N_{eff} = 2 \times 10^{20}$ cm^{-3} is used. In panel (b), $N_{eff} = 1 \times 10^{21}$ cm^{-3} and $\delta = 1$ nm are used. In panel (c), the basic parameters of different materials are listed in Table I, and $N_{eff} = 1 \times 10^{21}$ cm^{-3} and $\delta = 1$ nm are used. Unless stated, other parameters are the same as those used for calculations in Fig. 4.

induced by polarization reversal and also can tolerate more deep traps to be present without changing the HRS and LRS defined by the polarization state

(iv) Reducing the dead-layer thickness (δ)

(v) Attaining an appropriate dielectric constant of the dead layer (ε_{st_d}).

The last two approaches emphasize the importance of the properties of the dead layer, because they are crucial in determining the magnitudes of Schottky barrier modulations induced by both polarization reversal and charge injection and trapping [see Eqs. (3), (6), (8), (12) and (13)].

V. CONCLUSIONS

In summary, the effects of charge injection and trapping on the switchable diode-type RS behavior in ferroelectric diodes have been investigated both experimentally and theoretically. By using the SKPM technique, we have shown that the charge injection and trapping occur simultaneously with polarizations switching in the electrical poling process. In addition, the sample with high density of interfacial traps exhibits poor reproducibility and stability of hysteretic I-V characteristics, indicating that the RS behavior is significantly influenced by charge injection and trapping. A theoretical model has been proposed to describe the coeffect of polarization reversal and charge injection and trapping on ferroelectric diodes. It has been demonstrated that the trapped charges could modify the Schottky barrier in a way opposite to the polarization. As a result, various types of hysteretic I-V characteristics could be observed. In addition, the ER ratio, RS polarity, and the HRS and LRS initially defined by the polarization state could all be modified by the trapped charges. Our model, therefore, successfully extends the model of Pintilie *et al.* to explain the commonly observed RS phenomena in realistic ferroelectric diodes. Finally, several approaches that are useful to suppress the effect of charge injection and trapping and to further realize high-performance polarization-reversal-induced RS, have been proposed. The present work therefore sheds light on the microscopic mechanisms of polarization reversal and charge-trapping comodulated RS behavior in ferroelectric diodes, and also provides guidance for developing reliable ferroelectric RS memories.

ACKNOWLEDGMENTS

The authors would like to thank the National Key Research Program granted by Ministry of Science and Technology of the People's Republic of China (No. 2016YFA0201002 and No. 2016YFA0300101), the State Key Program for Basic Researches of China (No. 2015CB921202), National Natural Science Foundation of China (No. 51602110, No. 51272078, and No. 51431006), the Project for Guangdong Province Universities and Colleges Pearl River Scholar Funded Scheme (2014), the Science and Technology Planning Project of Guangdong Province (No. 2015B090927006), the Natural Science Foundation of Guangdong Province (No. 2016A030308019), and the International Science & Technology Cooperation Platform Program of Guangzhou (No. 2014J4500016).

[1] V. Garcia, S. Fusil, K. Bouzehouane, S. Enouz-Vedrenne, N. D. Mathur, A. Barthélémy, and M. Bibes, Giant tunnel electroresistance for non-destructive readout of ferroelectric states, Nature (London) **460**, 81 (2009).

[2] A. Gruverman, D. Wu, H. Lu, Y. Wang, H. W. Jang, C. M. Folkman, M. Ye. Zhuravlev, D. Felker, M. Rzchowski, C.-B. Eom, and E. Y. Tsymbal, Tunneling electroresistance effect in ferroelectric tunnel junctions at the nanoscale, Nano Lett. **9**, 3539 (2009).

[3] A. Chanthbouala, A. Crassous, V. Garcia1, K. Bouzehouane, S. Fusil, X. Moya, J. Allibe, B. Dlubak, J. Grollier, S. Xavier, C. Deranlot, A. Moshar, R. Proksch, N. D. Mathur, M. Bibes, and A. Barthélémy, Solid-state memories based on ferroelectric tunnel junctions, Nat. Nanotechnol. **7**, 101 (2011).

[4] T. Choi, S. Lee, Y. J. Choi, V. Kiryukhin, and S.-W. Cheong, Switchable ferroelectric diode and photovoltaic effect in $BiFeO_3$, Science **324**, 63 (2009).

[5] A. Q. Jiang, C. Wang, K. J. Jin, X. B. Liu, J. F. Scott, C. S. Hwang, T. A. Tang, H. B. Lu, and G. Z. Yang, A resistive memory in semiconducting $BiFeO_3$ thin-film capacitors, Adv. Mater. **23**, 1277 (2011).

[6] D. J. Kim, H. Lu, S. Ryu, C.-W. Bark, C.-B. Eom, E. Y. Tsymbal, and A. Gruverman, Ferroelectric tunnel memristor, Nano Lett. **12**, 5697 (2012).

[7] R. Soni, A. Petraru, P. Meuffels, O. Vavra, M. Ziegler, S. K. Kim, D. S. Jeong, N. A. Pertsev, and Hermann Kohlstedt, Giant electrode effect on tunnelling electroresistance in ferroelectric tunnel junctions, Nat. Commun. **5**, 5414 (2014).

[8] Y. B. Lin, Z. B. Yan, X. B. Lu, Z. X. Lu, M. Zeng, Y. Chen, X. S. Gao, J. G. Wan, J. Y. Dai, and J.-M. Liu, Temperature-dependent and polarization-tuned resistive switching in $Au/BiFeO_3/SrRuO_3$ junctions, Appl. Phys. Lett. **104**, 143503 (2014).

[9] M. Li, J. Zhou, X. Jing, M. Zeng, S. Wu, J. Gao, Z. Zhang, X. Gao, X. Lu, J.-M. Liu, and M. Alexe, Controlling resistance switching polarities of epitaxial $BaTiO_3$ films by mediation of ferroelectricity and oxygen vacancies, Adv. Electron. Mater. **1**, 1500069 (2015).

[10] H. Kohlstedt, A. Petraru, K. Szot, A. Rüdiger, P. Meuffels, H. Haselier, R. Waser, and V. Nagarajan, Method to distinguish ferroelectric from nonferroelectric origin in case of resistive switching in ferroelectric capacitors, Appl. Phys. Lett. **92**, 062907 (2008).

[11] P. W. M. Blom, R. M. Wolf, J. F. M. Cillessen, and M. P. C. M. Krijn, Ferroelectric Schottky Diode, Phys. Rev. Lett. **73**, 2107 (1994).

[12] L. Pintilie and M. Alexe, Metal-ferroelectric-metal heterostructures with Schottky contacts. I. Influence of the ferroelectric properties, J. Appl. Phys. **98**, 124103 (2005).

[13] L. Pintilie, I. Boerasu, M. J. M. Gomes, T. Zhao, R. Ramesh, and M. Alexe, Metal-ferroelectric-metal structures with Schottky contacts. II. Analysis of the experimental current-voltage and capacitance-voltage characteristics of $Pb(Zr, Ti)O_3$ thin films, J. Appl. Phys. **98**, 124104 (2005).

[14] H. T. Yi, T. Choi, S. G. Choi, Y. S. Oh, and S.-W. Cheong, Mechanism of the switchable photovoltaic effect in ferroelectric $BiFeO_3$, Adv. Mater. **23**, 3403 (2011).

[15] C. Wang, K. Jin, Z. Xu, L. Wang, C. Ge, H. Lu, H. Guo, M. He, and G. Yang, Switchable diode effect and ferroelectric resistive switching in epitaxial $BiFeO_3$ thin films, Appl. Phys. Lett. **98**, 192901 (2011).

[16] D. S. Jeong, R. Thomas, R. S. Katiyar, J. F. Scott, H. Kohlstedt, A. Petraru, and C. S. Hwang, Emerging memories: Resistive switching mechanisms and current status, Rep. Prog. Phys. **75**, 076502 (2012).

[17] Z. B. Yan and J.-M. Liu, Resistance switching memory in perovskite oxides, Ann. Phys. (Amsterdam) **358**, 206 (2015).

[18] A. Tsurumaki, H. Yamada, and A. Sawa, Impact of Bi deficiencies on ferroelectric resistive switching characteristics observed at p-Type Schottky-Like $Pt/Bi_{1-\delta}FeO_3$ Interfaces, Adv. Funct. Mater. **22**, 1040 (2012).

[19] H. Matsuo, Y. Kitanaka, R. Inoue, Y. Noguchi, and M. Miyayama, Switchable diode-effect mechanism in ferroelectric $BiFeO_3$ thin film capacitors, J. Appl. Phys. **118**, 114101 (2015).

[20] J. H. Lee, J. H. Jeon, C. Yoon, S. Lee, Y. S. Kim, T. J. Oh, Y. H. Kim, J. Park, T. K. Song, and B. H. Park, Intrinsic defect-mediated conduction and resistive switching in multiferroic $BiFeO_3$ thin films epitaxially grown on $SrRuO_3$ bottom electrodes, Appl. Phys. Lett. **108**, 112902 (2016).

[21] F. Pan, S. Gao, C. Chen, C. Song, and F. Zeng, Recent progress in resistive random access memories: materials, switching mechanisms, and performance, Mater. Sci. Eng. R **83**, 1 (2014).

[22] Y. Watanabe, Electrical transport through $Pb(Zr, Ti)O_3$ p-n and p-p heterostructures modulated by bound charges at a ferroelectric surface: Ferroelectric p-n diode, Phys. Rev. B **59**, 11257 (1999).

[23] See Supplemental Material at http://link.aps.org/supplemental/10.1103/PhysRevApplied.7.014020 for XRD θ-2θ scan, (103) and (113) RSMs, P-E and J-E curves measured with large-area Au electrodes, poling voltage-dependent SKPM and PFM images, and AFM images and Fe $2p$ XPS spectra of untreated and plasma-treated samples.

[24] H. Fan *et al.*, Large electroresistance and tunable photovoltaic properties in ferroelectric nanoscale capacitors based on ultrathin super-tetragonal $BiFeO_3$ films (to be published).

[25] S. V. Kalinin and D. A. Bonnell, Local potential and polarization screening on ferroelectric surfaces, Phys. Rev. B **63**, 125411 (2001).

[26] X. Q. Chen, H. Yamada, T. Horiuchi, K. Matsushige, S. Watanabe, M. Kawai, and P. S. Weiss, Surface potential of ferroelectric thin films investigated by scanning probe microscopy, J. Vac. Sci. Technol. B **17**, 1930 (1999).

[27] J. Y. Son, S. H. Bang, and J. H. Cho, Kelvin probe force microscopy study of $SrBi_2Ta_2O_9$ and $PbZr_{0.53}Ti_{0.47}O_3$ thin films for high-density nonvolatile storage devices, Appl. Phys. Lett. **82**, 3505 (2003).

[28] Y. Kim, C. Bae, K. Ryu, H. Ko, Y. K. Kim, S. Hong, and H. Shin, Origin of surface potential change during ferroelectric switching in epitaxial $PbTiO_3$ thin films studied by scanning force microscopy, Appl. Phys. Lett. **94**, 032907 (2009).

[29] H. Y. Yu, X. D. Feng, D. Grozea, Z. H. Lu, R. N. S. Sodhi, A-M. Hor, and H. Aziz, Surface electronic structure of plasma-treated indium tin oxides, Appl. Phys. Lett. **78**, 2595 (2001).

[30] I. Yagi, K. Tsukagoshi, and Y. Aoyagi, Modification of the electric conduction at the pentacene/SiO_2 interface by surface termination of SiO_2, Appl. Phys. Lett. **86**, 103502 (2005).

[31] D. D. Pollock, *Physical Properties of Materials for Engineers* (CRC Press, New York, 1993), Chap. 11, pp. 443–447.
[32] L. Pintilie, I. Vrejoiu, D. Hesse, G. LeRhun, and M. Alexe, Ferroelectric polarization-leakage current relation in high quality epitaxial $Pb(Zr,Ti)O_3$ films, Phys. Rev. B **75**, 104103 (2007).
[33] M. S. Tyagi, *Metal-Semiconductor Schottky Barrier Junctions and Their Applications* (Springer, New York, 1984), Chap. 1, pp. 33–34.
[34] H. Tabata, O. Murata, T. Kawai, S. Kawai, and M. Okuyama, *C*-axis preferred orientation of laser ablated epitaxial $PbTiO_3$ films and their electrical properties, Appl. Phys. Lett. **64**, 428 (1994).
[35] P. W. Peacock and J. Robertson, Band offsets and Schottky barrier heights of high dielectric constant oxides, J. Appl. Phys. **92**, 4712 (2002).
[36] A. Petraru, N. A. Pertsev, H. Kohlstedt, U. Poppe, R. Waser, A. Solbach, and U. Klemradt, Polarization and lattice strains in epitaxial $BaTiO_3$ films grown by high-pressure sputtering, J. Appl. Phys. **101**, 114106 (2007).
[37] B. H. Hoerman, G. M. Ford, L. D. Kaufmann, and B. W. Wessels, Dielectric properties of epitaxial $BaTiO_3$ thin films, Appl. Phys. Lett. **73**, 2248 (1998).
[38] K. Amanuma, T. Hase, and Y. Miyasaka, Preparation and ferroelectric properties of $SrBi_2Ta_2O_9$ thin films, Appl. Phys. Lett. **66**, 221 (1995).
[39] J. Wang, J. B. Neaton, H. Zheng, V. Nagarajan, S. B. Ogale, B. Liu, D. Viehland, V. Vaithyanathan, D. G. Schlom, U. V. Waghmare, N. A. Spaldin, K. M. Rabe, M. Wuttig, and R. Ramesh, Epitaxial $BiFeO_3$ multiferroic thin film heterostructures, Science **299**, 1719 (2003).
[40] L. Pintilie, C. Dragoi, Y. H. Chu, L. W. Martin, R. Ramesh, and M. Alexe, Orientation-dependent potential barriers in case of epitaxial Pt-$BiFeO_3$-$SrRuO_3$ capacitors, Appl. Phys. Lett. **94**, 232902 (2009).
[41] S. Iakovlev, C.-H. Solterbeck, M. Kuhnke, and M. Es-Souni, Multiferroic $BiFeO_3$ thin films processed via chemical solution deposition: Structural and electrical characterization, J. Appl. Phys. **97**, 094901 (2005).
[42] S. J. Clark and J. Robertson, Band gap and Schottky barrier heights of multiferroic $BiFeO_3$, Appl. Phys. Lett. **90**, 132903 (2007).
[43] Y. Du, H. Pan, S. Wang, T. Wu, Y. P. Feng, J. Pan, and A. T. S. Wee, Symmetrical negative differential resistance behavior of a resistive switching device, ACS Nano **6**, 2517 (2012).
[44] M. Dawber and J. F. Scott, Negative differential resistivity and positive temperature coefficient of resistivity effect in the diffusion limited current of ferroelectric thin film capacitors, J. Phys. Condens. Matter **16**, L515 (2004).
[45] L. Pintilie, V. Stancu, L. Trupina, and I. Pintilie, Ferroelectric Schottky diode behavior from a $SrRuO_3$-$Pb(Zr_{0.2}Ti_{0.8})O_3$-Ta structure, Phys. Rev. B **82**, 085319 (2010).
[46] Y. Shuai, S. Zhou, D. Bürger, M. Helm, and H. Schmidt, Nonvolatile bipolar resistive switching in $Au/BiFeO_3/Pt$, J. Appl. Phys. **109**, 124117 (2011).
[47] Y. Zhu, M. Li, Z. Hu, X. Liu, Q. Wang, X. Fang, and K. Guo, Nonvolatile resistive switching behaviour and the mechanism in $Nd:BiFeO_3/Nb:SrTiO_3$ heterostructure, J. Phys. D **46**, 215305 (2013).
[48] F. Liu, Y. Zhou, Y. Wang, X. Liu, J. Wang, and H. Guo, Negative capacitance transistors with monolayer black phosphorus, npj Quantum Mater. **1**, 16004 (2016).
[49] E. Mikheev, B. D. Hoskins, D. B. Strukov, and S. Stemmer, Resistive switching and its suppression in $Pt/Nb:SrTiO_3$ junctions, Nat. Commun. **5**, 3990 (2014).
[50] E. Mikheev, J. Hwang, A. P. Kajdos, A. J. Hauser, and S. Stemmer, Tailoring resistive switching in $Pt/SrTiO_3$ junctions by stoichiometry control, Sci. Rep. **5**, 11079 (2015).
[51] M. Grossmann, O. Lohse, D. Bolten, U. Boettger, and R. Waser, The interface screening model as origin of imprint in $PbZr_xTi_{1-x}O_3$ thin films. II. Numerical simulation and verification, J. Appl. Phys. **92**, 2688 (2002).
[52] C. Park, Y. Seo, J. Jung, and D.-W. Kim, Electrode-dependent electrical properties of metal/Nb-doped $SrTiO_3$ junctions, J. Appl. Phys. **103**, 054106 (2008).